EES Solar

PAPER

View Article Online
View Journal | View Issue

Cite this: *EES Sol.*, 2025, **1**, 1135

Molecular interactions and excited-state dynamics in MA free efficient and stable 2D/3D perovskite solar cells

Shivani Choudhary, [a] Naveen Kumar Tailor,[ad] Kapil Kumar,[bc] Rabindranath Garai, [a] Mohammad Adil Afroz [a] and Soumitra Satapathi *[ad]

Mixed 2D/3D perovskite solar cells (PSCs) achieve high efficiency and long-term stability, primarily driven by the critical role of functional groups on large organic molecules, which influence the underlying chemical interaction mechanisms. In this study, we explore the molecular interactions and excited-state dynamics of mixed 2D/3D PSCs based on a methylammonium-free (MA-free) FA-Cs perovskite structure, aimed at enhancing device performance and stability. We introduced benzamidine hydrochloride (BzCl) and 3,5-difluorobenzamidine hydrochloride (DFBzCl) molecules to form a 2D perovskite layer on top of the 3D perovskite absorber. Remarkably, the incorporation of DFBzCl resulted in a significant increase in power conversion efficiency (PCE), rising from 18.09% in the control device to 21.21%. In-depth excited-state dynamics analysis using ultrafast transient absorption spectroscopy revealed that BzCl and DFBzCl incorporation slows hot carrier cooling, facilitates charge transfer, mitigates phase segregation, and extends carrier recombination lifetimes. These effects are particularly pronounced in DFBzCl-modified devices due to the higher dipole moment of the molecule, which enhances internal electric fields, improves energy band alignment, and facilitates better charge transport at the interface. The study emphasizes the importance of dipole moment, and excited-state dynamics in optimizing the performance and stability of 2D/3D PSCs, providing crucial insights for future design.

Received 22nd July 2025
Accepted 15th October 2025

DOI: 10.1039/d5el00121h

rsc.li/EESSolar

Broader context

Hybrid 2D/3D perovskite solar cells have shown improved moisture stability and reduced ion migration, but the mechanisms underlying interactions between the 3D and 2D layers remain insufficiently understood. In this study, we explore the molecular interactions and excited-state dynamics of mixed 2D/3D PSCs based on a methylammonium-free (MA-free) FA-Cs perovskite, aimed at enhancing device performance and stability. By introducing benzamidine hydrochloride (BzCl) and 3,5-difluorobenzamidine hydrochloride (DFBzCl) as interfacial modifiers, we demonstrate a significant enhancement in power conversion efficiency (PCE), from 18.09% in the control to 21.21%, along with reduced hysteresis and improved stability. Ultrafast transient absorption spectroscopy reveals prolonged hot carrier cooling, redshifted ground-state bleach (GSB), and reduced spectral broadening, signifying enhanced band dispersion and defect passivation. These findings establish a direct correlation between dipole moments, excited-state dynamics, and charge transport mechanisms, providing a novel approach for the rational design of high-performance and stable perovskite solar cells.

1 Introduction

Hybrid perovskite solar cells (PSCs) have emerged as a leading photovoltaic technology, with power conversion efficiencies (PCEs) reaching 27%.[1–3] Despite PSC's spectacular PCEs, their performance is often limited by long-term stability posing a challenge for commercialization.[4,5] To realize the coexistence of high efficiency and ultra stability in PSCs, researchers began to construct 2D/3D perovskites by surface passivation.[6–9] The formation of a 2D layer on top of the 3D perovskite can effectively passivate the perovskite defects at the interface between the perovskite and charge transporting layers, leading to an improvement in device performance.[10–12] Giovanni Pica *et al.* studied the impact of surface passivation on p-i-n PSCs using thiophene-based cations and found that surface passivation significantly improves device performance, achieving a 23.56% efficiency, reduced voltage losses, and increased fill factor.[12] The cation's chemical structure determines passivation efficacy, improving energy level alignment and reducing nonradiative recombination. The interfacial dipole layer is a popular strategy in surface engineering for PSCs, as it can alter the electronic band structure and adjust charge transport.[13,14] The amidino-based ligands have an optimal size and abundant N–H

[a]*Department of Physics, Indian Institute of Technology Roorkee, Roorkee 247667, India. E-mail: soumitra.satapathi@ph.iitr.ac.in*
[b]*CSIR-National Physical Laboratory, Dr K.S. Krishnan Marg, New Delhi 110012, India*
[c]*Academy of Scientific and Innovative Research (AcSIR), Ghaziabad 201002, India*
[d]*Center for Sustainable Energy, Indian Institute of Technology Roorkee, Roorkee 247667, India*

structures, enabling multiple hydrogen bonds with the $[PbI_6]^{4-}$ octahedra, making them superior to conventional amino-based ligands. Yue *et al.* used interfacial dipole layers as a surface engineering strategy for PSCs, achieving a PCE of 24% using 4-(trifluoromethyl) benzamidine hydrochloride (TFPhFACl) to construct a 2D capping layer on a 3D perovskite.[15] This enhancement was due to the formation of a dipole layer by $TFPhFA^+$ cations and the coordination of these cations with Pb–I octahedra. Qiu *et al.* conducted first-principles calculations to investigate the dipole moment of phenethylamine-type molecules in 2D/3D perovskites, demonstrating that it can be tuned by varying the number of fluorine atoms on the para position of the benzene ring.[16] Xinran Xu *et al.* have studied that by introducing fluorine at *meta* positions on the benzene ring suppresses the penetration of the 2D perovskite phase, resulting in improved charge transport and further enhances the device stability. Therefore, *meta*-substituted ligand exhibited the greatest steric hindrance because of its distinct molecular configuration, which effectively restricted its penetration into the 3D perovskite layer.[17] Furthermore, fluorine atoms exhibit electronic effects, orthorhombicity, and low steric hindrance, which improve intermolecular stacking and interactions with the perovskite, enhancing charge transport and reducing charge trapping at the interface. These advancements highlight the ongoing efforts to overcome challenges and further enhance the efficiency and durability of 2D/3D PSCs.[6–10]

Hybrid 2D/3D perovskite architectures have shown improved moisture stability and reduced ion migration, but the mechanisms underlying interactions between the 3D and 2D layers remain insufficiently understood.[18,19] Fluorine-substituted organic functional groups, characterized by their high electronegativity, are effective as 2D capping layers, modulating the kinetics of interfacial charge extraction.[20–22] These layers enhance photophysical properties by improving exciton confinement, reducing nonradiative recombination, and supporting efficient charge carrier dynamics, thereby boosting device stability and performance. Despite these advancements, critical questions about the physics of the 2D/3D interface persist. Detailed photophysical studies are essential to comprehensively understand molecular interactions at the 2D/3D interface, which is vital for designing high-performance inverted PSCs.[23–25] Moreover, understanding mechanisms like hot carrier cooling, charge transfer, and the relationship between morphology, structure, and excited-state dynamics in 2D/3D PSCs is crucial.[26–31] Investigating these aspects, particularly excited-state dynamics, is key to unlocking the full potential of these hybrid systems for achieving high-efficiency solar cells.

In this study, we developed a methylammonium-free (MA-free) FA-Cs-based 3D perovskite absorber (control) and used benzamidine hydrochloride (BzCl) and 3,5-difluorobenzamidine hydrochloride (DFBzCl) passivation on top of the 3D perovskite structure. To investigate the impact of these organic spacer-based 2D layers, we performed comprehensive structural, elemental, and optical characterizations using X-ray diffraction (XRD), X-ray photoelectron spectroscopy (XPS), ultraviolet photoelectron spectroscopy (UPS), field-emission scanning electron microscopy (FESEM), and Kelvin probe force microscopy (KPFM), absorption and time-resolved photoluminescence spectroscopy. Subsequently, PSCs were fabricated using the control 3D perovskite and 2D/3D perovskite incorporating BzCl and DFBzCl. A significant enhancement in device performance was observed with the DFBzCl-modified 2D/3D perovskite, resulting in an efficiency increase from 18.09% (control) to 21.21%. This improvement is attributed to the higher dipole moment of DFBzCl, which enhances the internal electric field, improves morphology and crystallinity, and suppresses interfacial recombination. Mott–Schottky analysis revealed an enhanced built-in potential and a reduced defect density in the DFBzCl-based devices compared to the control. Impedance spectroscopy further demonstrated increased interfacial recombination resistance and reduced ion accumulation at the interface in DFBzCl-modified devices. Additionally, time-correlated single-photon counting (TCSPC) measurements showed a longer carrier decay lifetime in DFBzCl-based devices compared to the control, indicating prolonged charge carrier lifetimes and reduced recombination. These improvements in built-in potential, recombination resistance, and carrier lifetime collectively contribute to more efficient charge transport, reduced carrier losses, and overall enhanced device performance. To further elucidate the underlying mechanisms, we investigated the excited-state dynamics using ultrafast transient absorption spectroscopy, focusing on the interactions between the 2D and 3D perovskite layers. This analysis revealed how the incorporation of BzCl and DFBzCl influences key processes such as hot carrier cooling, charge transfer, recombination dynamics, and phase segregation effects. The findings of this study underscore the critical role of optimizing dipole moments, molecular interactions, and charge dynamics for enhancing both efficiency and stability in PSCs. These insights offer valuable guidance for the rational design of high-performance solar cells and contribute to a deeper understanding of the underlying photophysical pathways that govern device operation.

2 Results and discussion

2.1 Chemical structure, structural and optical characteristics

We introduce methylammonium (MA)-free 3D perovskite films composed of $FA_{0.9}Cs_{0.1}PbI_{2.8}Br_{0.2}$, with details of their preparation provided in the SI. The composition of $FA_{0.9}Cs_{0.1}PbI_{2.8}Br_{0.2}$ was optimized, and films were fabricated *via* the spin coating method. The MA-free composition results as stable composition (named "control" here) than the including MA cations.[1] Furthermore, we have fabricated the 2D perovskite layer on the top of this 3D control composition using the BzCl and DFBzCl organic spacers. The solution of molecules BzCl and DFBzCl were used to fabricate the 2D layer on the control film. The chemical structure of both molecules is shown in Fig. 1a. Firstly, we have calculated the electrostatic potential (ESP) profile of both molecules to get insights into dipole moment and polarization. The obtained ESP profile is shown in Fig. 1b.

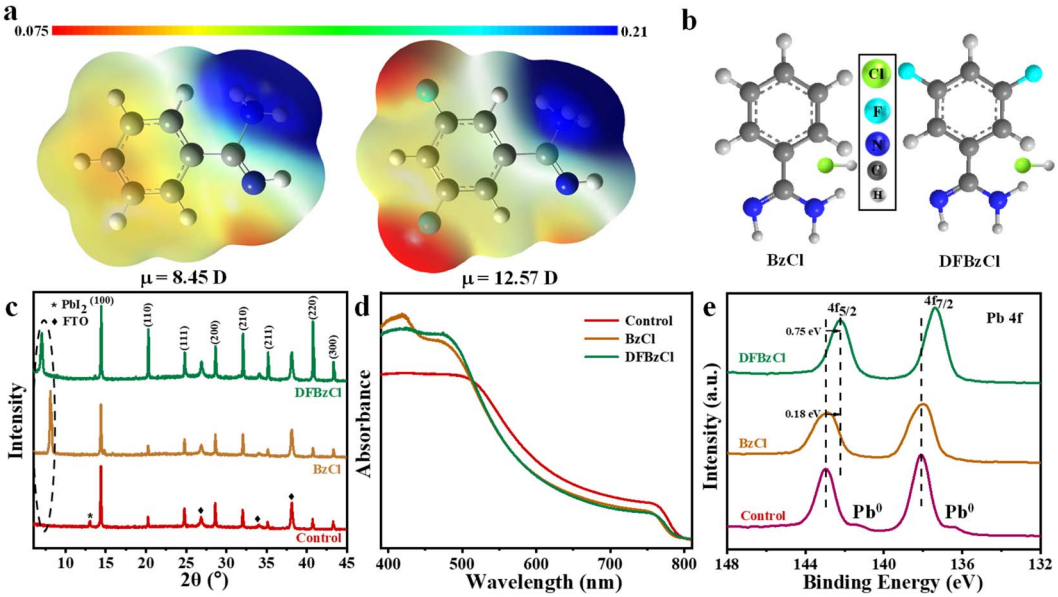

Fig. 1 (a) The electrostatic potential map and local dipole moment of BzCl and DFBzCl organic spacers. (b) The chemical structures of BzCl and DFBzCl. (c) XRD pattern and (d) absorption spectra of pristine and modified films. (e) XPS profile of control and BzCl and DFBzCl modified films.

ESP mapping using density functional theory (DFT) was performed to understand the interactions between fluorine and organic amines with the 3D perovskite structure (Fig. 1a). The ESP mapping and electric dipole moments of BzCl and DFBzCl are shown in Fig. 1a and b. The color scale, from red to blue, represents the shift from electron-rich (negatively charged) regions to electron-deficient (positively charged) areas within the molecules. The dipole moment of BzCl is calculated to be 8.45 debye, while DFBzCl exhibits a higher dipole moment of 12.57 debye. The increased dipole moment of DFBzCl suggests that the negative charge is primarily localized on the fluorine atoms, enhancing the molecule's electronic polarity.[15] In DFBzCl, the fluorine atom and the $-NH_3$ group are positioned para to each other, leading to higher electron density and a more negative surface potential.[32] This configuration enhances the molecule's ability to passivate acceptor defects in the perovskite film, especially by interacting with both positive (Pb^{2+}) and negative (I^-) defects.[33] The theoretical insights provided by DFT were further investigated experimentally to assess the effects of BzCl and DFBzCl on perovskite device performance.[34]

To investigate the impact of BzCl and DFBzCl on crystal growth, X-ray diffraction (XRD) measurements were conducted on both control (3D) and surface-treated perovskite films, varying the ligand concentrations (Fig. S1a and b). As shown in Fig. 1c, no significant shift in the XRD diffraction peaks was observed after surface treatment, indicating that the BzCl and DFBzCl ligands did not alter the underlying perovskite phase or crystal structure. However, prominent diffraction peaks at $2\theta < 10°$ were detected in the surface-treated films, which can be attributed to the formation of a quasi-2D or 2D perovskite phase atop the 3D perovskite layer. XRD patterns were also obtained for films treated with varying ligand concentrations (1 mg mL^{-1} to 3 mg mL^{-1}). As the concentration of BzCl and DFBzCl increased, a new diffraction peak emerged at a low angle, and its intensity was enhanced with increasing ligand concentration (Fig. S1). To confirm the origin of these low-angle diffraction peaks, we prepared films of BzCl:PbI_2 and DFBzCl:PbI_2, referred to as 2D films (Fig. S2). These peaks, observed at 8.1° for BzCl-treated films and 7° for DFBzCl-treated films, are characteristic of 2D perovskite structures.[35] This indicates the formation of a mixed-halide 2D compared to their phase-pure counterparts perovskite layer on top of the 3D perovskite.[36] This suggests that BzCl and DFBzCl interact with un-coordinated PbI_2 on the 3D perovskite surface to form a stable 2D perovskite layer. Additionally, the post-treatment led to a gradual attenuation of the PbI_2 diffraction peak at 12.90°, further supporting the idea that the 2D layer forms through interaction between the organic spacers and the excess PbI_2 in the 3D perovskite.[37,38]

We have further investigated the optical properties of the perovskite films by measuring their absorption spectra to understand the impact of the organic spacers (Fig. 1d and S3). The absorption spectra of the control, BzCl-, and DFBzCl-treated films with varying concentrations displayed similar profiles, with an absorption onset around 790 nm. As the concentration of the ligands increased, the absorption intensity at lower wavelengths initially increased up to 2 mg mL^{-1} but decreased at 3 mg mL^{-1}, suggesting that the addition of BzCl and DFBzCl improves film morphology up to an optimal concentration of 2 mg mL^{-1}.[39] Notably, the absorption spectra remained largely unchanged, with a slight blue shift in the onset for BzCl- and DFBzCl-treated films compared to the control, indicating a marginal increase in bandgap (Fig. 1d). Tauc plot analysis confirmed a slight bandgap increase from 1.57 eV in untreated films to 1.58 eV in films treated with 2 mg mL^{-1} of BzCl and DFBzCl (Fig. S4).[35] A similar small peak

around 430 nm was also observed in the surface-treated films (Fig. 1d), indicating the successful formation of a quasi-2D or 2D perovskite phase atop the 3D perovskite.[32] This highlights the role of BzCl and DFBzCl in modulating the optical properties and confirming the formation of a 2D perovskite layer. Moreover, the photoluminescence (PL) spectra of the control, 2 mg mL^{-1} BzCl-, and 2 mg mL^{-1} DFBzCl-treated films were analyzed to assess the impact of surface treatment on the carrier dynamics of the perovskite films (Fig. S5). The control film exhibited a PL emission peak around 795 nm, characteristic of 3D perovskite emission. In contrast, the BzCl- and DFBzCl-treated films showed significantly enhanced PL intensities, with blue-shifted emission peaks at 779 nm and 773 nm, respectively. The increase in PL intensity indicates improved film quality and a substantial reduction in defect-mediated recombination, which is typically caused by surface defects. The observed blue shift in the PL emission peaks for BzCl- and DFBzCl-treated films can be attributed to the formation of low-dimensional 2D or quasi-2D perovskite phases, which is related with the XRD and UV-vis results. Additionally, both treated films displayed small excitonic peaks in the 500–620 nm range, corresponding to PL emission from quasi-2D perovskites with different *n*-values.

To further investigate the chemical interactions of BzCl and DFBzCl on the surface of perovskite films, X-ray photoelectron spectroscopy (XPS) analysis was performed. The XPS spectra of the control perovskite film, shown in Fig. 1e, display two main peaks at binding energies of 138.10 eV and 142.96 eV, corresponding to the Pb $4f_{7/2}$ and Pb $4f_{5/2}$ core levels, respectively. These peaks are associated with Pb^{2+} ions in the Pb–I octahedra. Additionally, the control sample reveals two smaller peaks at 141.34 eV and 136.34 eV, which are attributed to Pb^0 defects. These Pb^0 impurities arise from the decomposition of PbI_2 under X-ray exposure, leading to defects that promote non-radiative recombination and degrade device performance. In contrast, the BzCl-treated perovskite film exhibits a slight shift in the Pb 4f peaks to lower binding energies (by ~0.18 eV), suggesting weak interaction between BzCl and the perovskite surface. This indicates a mild passivation effect, where BzCl interacts with the Pb^{2+} ions without significantly altering the electronic environment of the perovskite. The DFBzCl-treated film, however, shows a more pronounced shift in the Pb 4f peaks (by ~0.75 eV) toward lower binding energies. This larger shift indicates a stronger interaction between DFBzCl and the perovskite surface, which is attributed to the formation of N–H···I hydrogen bonds between the NH_3^+ group in DFBzCl and the $[PbI_6]^{4-}$ octahedra.[40] This interaction leads to the formation of a low-dimensional perovskite layer atop the passivated 3D perovskite, altering the electron cloud overlap between Pb–I and N–H bonds. This shift is due to the lone pair of electrons on the nitrogen (N) atom in DFBzCl coordinating with Pb^{2+}, strengthening the bond and improving surface passivation.[15,41]

Moreover, the Pb^0 defect peaks are completely suppressed in both BzCl- and DFBzCl-treated films, indicating that the chemical reactions between these ligands and residual PbI_2 significantly reduce the presence of these detrimental defects. This suggests improved material stability and reduced non-radiative recombination pathways, which would enhance the performance of PSCs. The full XPS survey, including spectra for the I 3d, N 1s, Cs 3d, Cl 2p, and Br 3d levels, is displayed in Fig. S6a. In particular, Fig. S6b shows that the I 3d core level for both BzCl- and DFBzCl-treated films shifts toward lower binding energy, indicating strong interactions between the organic spacers and iodine ions (I^-). The positively charged NH_3^+ groups in BzCl and DFBzCl are capable of forming hydrogen bonds with I^-, donating electron density to the iodine atoms.[10,15,42] This increases the outer electron cloud density and enhances the shielding effect, stabilizing the perovskite structure. Additionally, binding energies of other elements such as 'N' (Fig. S6c) and 'Cs' (Fig. S6d) also shift toward lower energies in the treated films, further confirming strong chemical interactions with the organic ligands. Interestingly, no significant shift is observed in the binding energies for 'Br' or 'Cl', indicating that the primary interactions occur with the iodine ions and not with other halides (Fig. S6e and f). This XPS analysis reveals how the surface treatment with BzCl and DFBzCl alters the chemical environment of the perovskite films. The shifts in binding energy, particularly for Pb and I, reflect changes in the electronic structure and suggest improved passivation and defect reduction. DFBzCl, with its higher dipole moment, demonstrates stronger interactions with the perovskite surface, contributing to the formation of a 2D perovskite layer that enhances the material's stability and charge transport properties.

In addition to XPS, we measured the UPS spectra to calculate the energy levels and Fermi levels, providing insight into the electron and hole transport characteristics of the control and modified perovskite films in combination with electron transport layer (ETL) and hole transport layer (HTL) layers.[43] The obtained spectra are shown in Fig. S7. The cutoff, onset, and bandgap values used for these calculations are presented in Table S1. The control perovskite exhibits valence band maximum (VBM), Fermi level (E_f), and conduction band minimum (CBM) values of −5.64, −4.14, and −4.07 eV, respectively, indicating its n-type nature. In comparison, the BzCl-modified 2D/3D film shows VBM, E_f, and CBM levels of −5.73, −4.18, and −4.15 eV, respectively. Similarly, for the DFBzCl-modified film, the levels are −5.76, −4.19, and −4.18 eV, confirming an n-type nature for all three films, with an increased electron concentration in the modified perovskites.[43]

The schematic band structure for the device architecture is illustrated in Fig. S7c. The Fermi levels of the BzCl- and DFBzCl-treated films increased by 0.04 and 0.05 eV, respectively, compared to the control film, which implies more pronounced n-type characteristics at the upper surface. This increase in the Fermi level enhances the efficiency of charge extraction and transport from the perovskite to the ETL. This shift is likely due to the higher dipole moment of the fluorine-containing DFBzCl, which enhances the internal electric field. Furthermore, the CBM of the DFBzCl-modified 2D/3D perovskite is closer to the PCBM ETL layer, suggesting a higher probability of electron transfer from the perovskite to the ETL than in the BzCl-modified or control films. Additionally, the stepped energy

level arrangement of the perovskite below the HTL promotes efficient hole extraction while inhibiting electron transport to the HTL. The 2D/3D junction forms an n–n isotype heterojunction, commonly used to induce a back-surface field, improving electron transport across the junction.[44] The energy level gradient formed between the perovskite with ETL and HTL is important because it helps in separating electrons and holes efficiently.[7,32,35] This reduces recombination and improves the extraction of charge carriers, which directly impacts the open-circuit voltage (V_{OC}) and PCE of the device.

2.2 Morphology of control and modified films

The chemical interactions in perovskite materials significantly influence surface morphology through minor alterations in molecular configurations. To investigate this, we examined the surface morphology of control films and those modified with varying amounts of BzCl and DFBzCl. Our analysis revealed that the incorporation of a 2D perovskite layer, based on BzCl and DFBzCl, resulted in the formation of small laminae connecting the grains, unlike the control film, which consisted of larger grains with uneven grain distribution (Fig. 2a). This uneven grain morphology in the control film promotes carrier localization and trapping. In contrast, the BzCl and DFBzCl-modified films displayed uniform, tightly packed grains without noticeable pinholes, and the average grain size distribution increased in the DFBzCl perovskite film (Fig. 2b, c and S8).[10,13,15,32,41] Moreover, varying the concentration of these organic spacers led to the formation of plate-like crystals on the film surface, suggesting the emergence of 2D perovskite, as shown in Fig. S9. DFBzCl molecules exhibit stronger dipole interactions, enhancing electrostatic interactions with perovskite surfaces, resulting in better molecular layer alignment. The addition of BzCl and DFBzCl layers also regulated crystallization dynamics. The dipole moment of these molecules influenced crystal growth by modulating surface energy and nucleation dynamics, which in turn affected grain formation and packing. The DFBzCl-modified film exhibited a denser and more uniform grain distribution compared to BzCl, contributing to improved carrier delocalization and reduced carrier trapping at grain boundaries. Additionally, this top layer may improve the interface with the ETL, enhancing carrier extraction and reducing interfacial recombination losses, thereby driving improved device performance. Furthermore, the dense grain packing and DFBzCl coating provide better protection against moisture penetration and ionic transport, enhancing both the environmental and photostability of the devices.

Kelvin probe force microscopy (KPFM) was employed to further investigate surface roughness and potential

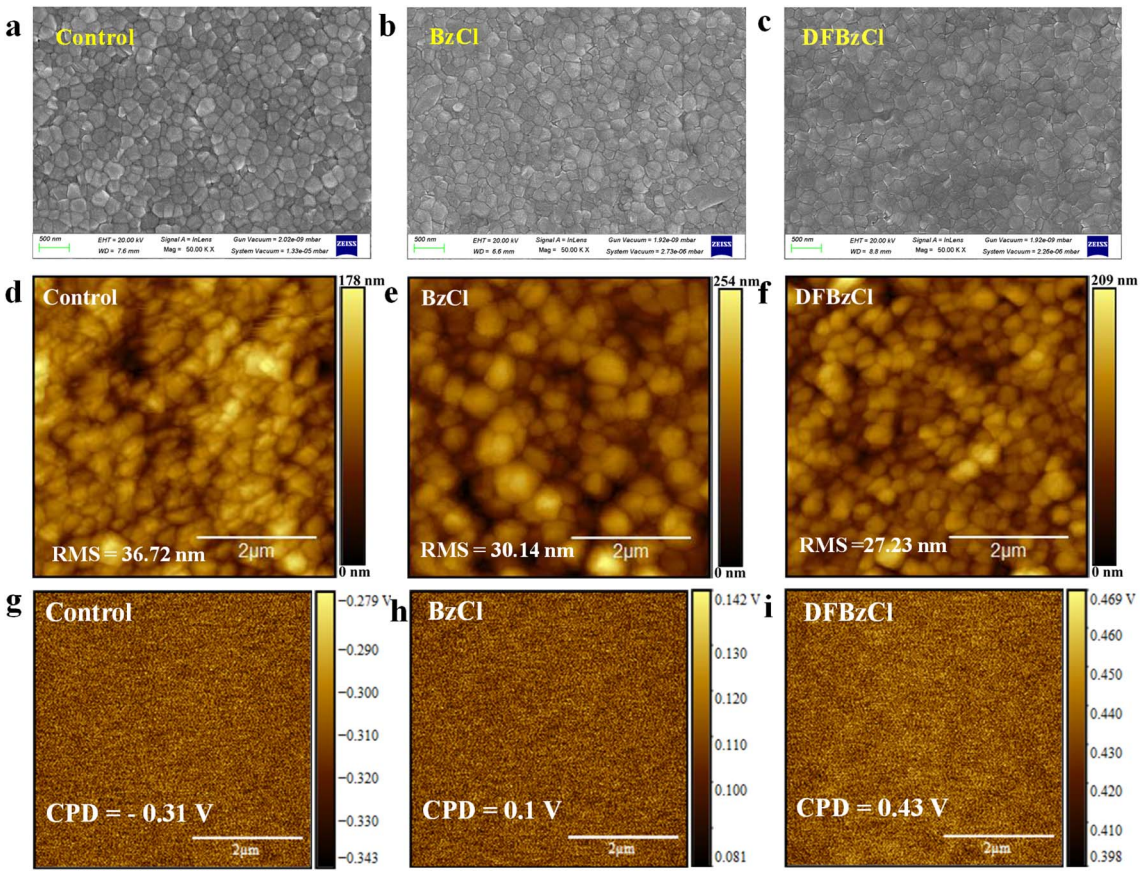

Fig. 2 Top-view FESEM images of perovskite films for (a–c) control (3D), BzCl, DFBzCl-treated 2D/3D films. The amount of organic spacers used is 2 mg ml^{-1} (d–f) the KPFM morphology maps of Control, BzCl-, DFBzCl-treated perovskite films and (g–i) CPD mappings (obtained from KPFM, 5.0 × 5.0 μm^2) of control, BzCl-, DFBzCl-treated films perovskite films.

distribution, as illustrated in Fig. 2d–f. The surface roughness measurements revealed values of 36.72 nm for the control sample, which decreased to 30.14 nm for the BzCl-treated sample and 27.23 nm for the DFBzCl-treated sample, with roughness distribution shown in Fig. S10. This reduction in roughness indicates an improved interfacial contact between the 2D/3D perovskite films and the electron transport layer (ETL), suggesting enhanced surface smoothness and crystallization quality in the BzCl- and DFBzCl-modified films.[38] The KPFM distribution images and surface potential (Fig. 2g–i and S11) further support this improvement of the modified 2D/3D perovskite films. The KPFM results also showed that the 2D/3D perovskite films exhibited a more uniform and higher potential distribution compared to the pure 3D perovskite films. The average surface potential of DFBzCl film exhibited a higher contact potential difference (CPD) of 0.43 V than the control film (−0.31 V) and BzCl film (0.1 V) which is consistent with reduced surface roughness.[10,35,44,45] Additionally, the DFBzCl-treated film exhibited higher surface potential than both the control and BzCl-treated films, which mitigates the accumulation of surface electrons and improves charge transport across the film. The alignment of molecular dipoles from BzCl and DFBzCl molecules likely contributes to this improvement by raising the work function, thereby facilitating more efficient charge transfer at the interface between the perovskite and the selective layers.

2.3 Device performance and carrier decay

We fabricated p-i-n structured PSCs with the device architecture FTO/NiO_x/MeO-2PACz/Perovskite/PCBM/BCP/Ag (inset of Fig. 3a). The cross-section SEM of the device is shown in Fig. S12 showing the presence of each layer. In the control devices, an MA-free perovskite was employed as the active layer. For the modified devices, a 2D perovskite layer was deposited over the 3D perovskite using BzCl and DFBzCl organic spacers, as described in the previous sections on film fabrications. The detailed device fabrication process is provided in the methods section. We measured the photovoltaic performance of these devices to examine the effect of the 2D perovskite layer on the control 3D perovskite devices. The *J*–*V* characteristics of the control 3D device and the BzCl and DFBzCl-modified 2D/3D devices are presented in Fig. 3a, while the key photovoltaic parameters for the champion devices are summarized in Table 1. The control PSC demonstrates a PCE of 18.09%, with a short-circuit current density (J_{SC}) of 23.6 mA cm^{-2}, an open-circuit voltage (V_{OC}) of 1.03 V, and a fill factor (FF) of 74.6%. Upon incorporating BzCl into the 2D/3D perovskite structure, the PCE improves to 19.54%. This enhancement is primarily attributed to a 29 mV increase in the V_{OC} and an improved FF. Further optimization using DFBzCl in the 2D/3D perovskite structure boosts the PCE to 21.21%. This improvement is associated with an increase in the V_{OC} to 1.08 V, a 57 mV enhancement compared to the control device. Additionally, the J_{SC} rises to 24.72 mA cm^{-2}, and the FF increases to

Table 1 Solar cell parameters of control 3D, and modified 2D/3D devices

Device/parameters	V_{OC} (V)	J_{SC} (mA cm^{-2})	FF (%)	PCE (%)
Control	1.031	23.65	74.2	18.09
BzCl	1.060	23.52	78.4	19.54
DFBzCl	1.088	24.72	78.9	21.21

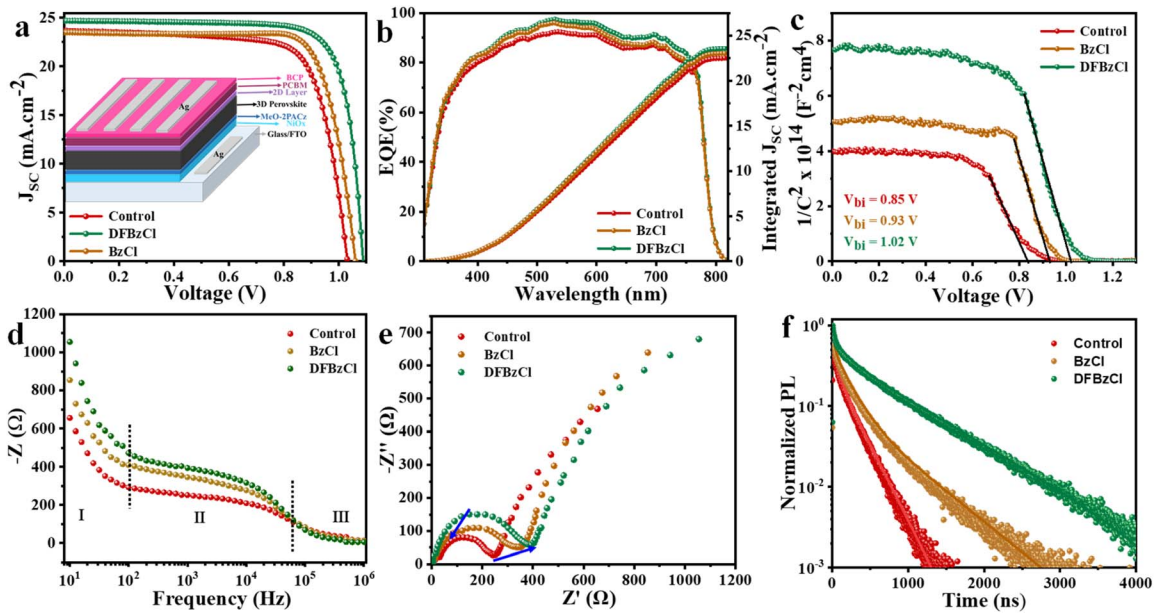

Fig. 3 (a) *J*–*V* characteristics of the control device and modified with BzCl and DFBzCl devices (inset: device architecture). (b) External quantum efficiency (EQE) and integrated current density as a function of wavelength for all three devices. (c) Mott–Schottky curve, (d) Bode plot with frequency (e) Nyquist plot for control, BzCl and DFBzCl devices under illumination. (f) Time-resolved PL curve for all three films measured by time-correlated single photon counting (TCSPC) measurement.

78.9%. Interfacial dipoles shift the energy alignment as discussed above optimizing charge transfer and increasing J_{SC} and FF. Further the significant increase in V_{OC} can be attributed to the higher dipole moment of DFBzCl, as calculated from the ESP profile.

This higher dipole moment enhances the internal electric field, leading to improved energy band alignment, thus facilitating better charge extraction and reducing recombination losses, which ultimately contributes to improved device performance. The obtained device parameters are shown in Table 1. The performance of fabricated devices using varying amounts of BzCl and DFBzCl is presented in Fig. S13, revealing that devices incorporating 2 mg of BzCl and 2 mg of DFBzCl demonstrate the most favorable results. Based on these findings, devices utilizing the 2 mg BzCl and 2 mg DFBzCl formulations were selected for subsequent characterizations and analyses. The improved performance observed in the DFBzCl 2D layer-based devices can be attributed to the inherent properties of DFBzCl. Specifically, DFBzCl molecules contribute to enhanced film morphology and reduced roughness, as evidenced by KPFM measurements. These improvements likely lead to better interfacial contact within the perovskite film and between the perovskite and adjacent layers, thereby facilitating more efficient charge transport and reduced charge recombination, which are critical factors influencing device performance in perovskite devices.

Hysteresis is a commonly observed phenomenon in PSCs that can impact the maximum power point (MPP) tracking, leading to inaccurate performance measurements. To assess this effect, we measured the forward and reverse J–V scans of all three device types. The DFBzCl-modified 2D/3D PSCs exhibited a significantly lower hysteresis index (1.51%) compared to the BzCl-modified (2.94%) and control devices (3.09%) as shown in Fig. S14. This reduction in hysteresis can be attributed to the higher dipole moment of DFBzCl, which improves the interface with the perovskite layer and suppresses ion migration. Additionally, the enhanced morphology and crystallinity of the modified devices further reduce hysteresis by minimizing ionic migration pathways and promoting better carrier delocalization. This leads to more stable device operation and higher performance stability under varying scan conditions. To verify the reproducibility and variations in device performance, statistical distributions for 15 devices are presented using box charts for the control (3D), BzCl, and DFBzCl-modified 2D/3D perovskite devices (Fig. S15). The average variation in all device parameters *i.e.* PCE, J_{SC}, V_{OC}, and FF is minimized for the DFBzCl-modified 2D/3D devices, as shown in Fig. S15a–d. Notably, the device-to-device V_{OC} variation is smaller in the DFBzCl-modified 2D/3D devices (Fig. S15c), indicating stable band alignment, enhanced built-in voltage, minimized fluctuations in quasi-Fermi level splitting (QFLS), and reduced non-radiative and interfacial recombination losses. Moreover, the dependency of V_{OC} at different light intensities as shown in Fig. S16a allows for the calculation of the ideality factor (n_{id}) using the equation:

$$n_{id} = \frac{q}{k_B \times T} \times \frac{dV_{oc}}{d(\ln(I))} \quad (1)$$

where T is the temperature of the system in Kelvin, k_B is the Boltzmann constant, q is the elementary charge constant, and I is the light intensity. The value of n_{id} for the control device decreased from 1.20 to 0.93 $(k_BT)/q$ after DFBzCl-treated PSCs. This suggests the DFBzCl-modified devices effectively minimized trap-assisted Shockley–Read–Hall (SRH) monomolecular recombination losses. The enhancing V_{OC} and FF in DFBzCl-treated devices indicates that DFBzCl reduces charge transport and trap-assisted nonradiative losses. This improvement reflects the stability and reproducibility of these devices. Further, we performed light-intensity dependent measurements of the J_{SC} for the DFBzCl-modified device. The results revealed that J_{SC} scales nearly linearly with the incident light intensity, with a power-law exponent of approximately 0.94 (Fig. S16b). This linear relationship strongly indicates the absence of significant bimolecular recombination or trap-assisted recombination losses under operating conditions. The stability of the devices was tested in a nitrogen-controlled environment over a period of 90 days. After the storage period, the control device retained 65% of its initial efficiency, while the DFBzCl-modified device retained 85% of its efficiency, as shown in Fig. S17. XRD and PL studies reveal that control 3D perovskite films undergo slight PbI_2 formation and PL degradation under light soaking, indicating defect-assisted degradation (Fig. S18). In contrast, DFBzCl-derived 2D/3D films show suppressed PbI_2 peaks, stable PL intensity, and no new emission peaks, confirming the absence of halide segregation. The 2D overlayer mitigates phase separation by acting as a barrier to ion migration and passivating defects, thereby enhancing structural stability and long-term operational robustness.

To validate the photoresponse of the devices, external quantum efficiency (EQE) measurements were conducted for all three device types, as shown in Fig. 3b. The modified 2D/3D devices show increased EQE in the range of 300 to 800 nm, indicating enhanced carrier absorption and collection, as well as reduced non-radiative recombination and thermal losses, as revealed by the EQE spectra. The EQE spectra closely align with the absorption range of the pristine films for the control, BzCl, and DFBzCl-modified perovskite layers, directly corresponding to the carrier absorption range and the generation of photoexcited electron–hole pairs (Fig. S19). The highest EQE was observed in the DFBzCl-modified devices, resulting in an integrated J_{SC} of 23.6 mA cm^{-2}. The integrated J_{SC} values were calculated as 22.5 mA cm^{-2} and 23 mA cm^{-2} for the control and BzCl-modified devices, respectively. The 2D layer formed by DFBzCl molecules effectively transports carriers, reduces defect states, and creates a better interface for enhanced carrier collection, which is attributed to improved morphology and crystallinity. Additionally, the enhanced dipole moment of DFBzCl promotes greater electron delocalization, supported by reduced grain boundaries and an increased built-in potential and QFLS under illumination. The improved EQE is directly linked to the superior performance of the DFBzCl-modified 2D/3D PSCs. The reduced thermal and non-radiative

recombination losses observed in the EQE spectra further support the enhanced device performance.

We further measured the Mott–Schottky response of these devices to investigate the underlying reason for the enhanced V_{OC} and other device performance parameters. The built-in potential (V_{bi}) was determined from the Mott–Schottky plot (Fig. 3c) by estimating the *X*-axis intercept for the control and modified 2D/3D devices. The DFBzCl-based device exhibited a higher V_{bi} of 1.02 V, compared to the BzCl-based device (0.93 V) and the control device (0.85 V). DFBzCl exhibits a higher dipole moment compared to BzCl, which enhances the internal electric field at the interface, thereby increasing the V_{bi}. This stronger dipole-induced field in DFBzCl-based devices leads to improved energy level alignment, resulting in a higher V_{bi}. The elevated built-in potential strengthens the driving force for charge extraction and exciton transfer within the electric field, contributing to the observed improvement in V_{OC} for the 2D/3D devices compared to the control device. Moreover, the enhancement in V_{bi} suggests a reduction in non-radiative recombination processes, which minimizes energy losses and improves overall device efficiency. The formation of a 2D perovskite layer atop the 3D perovskite, as confirmed by XRD and absorption spectra, further enhances charge carrier confinement and surface passivation. These combined effects result in an increased built-in potential, particularly in the DFBzCl-treated films, leading to the superior performance of these devices. This was further confirmed by interfacial charge density (*N*) obtained from the slope of Mott–Schottky plots. The control devices have the *N* value of 1.08×10^{16} cm^{-3} which gets suppressed to 0.90×10^{16} cm^{-3} for BzCl modified 2D/3D devices and 0.30×10^{16} cm^{-3} for DFBzCl modified 2D/3D devices, indicating a reduction in charge accumulation and better charge transport from the active layer to transport layers.

Moreover, we measured the impedance response of 3D and 2D/3D PSCs under illumination across a frequency range of 1 MHz to 10 Hz. Fig. 3a shows the representative Bode plot (Z′–f), while Fig. 3b presents the Nyquist plot (Z′–Z″) of the impedance spectra. In the Nyquist plot, at high frequencies, a small semicircle is observed, whereas at lower frequencies, a larger arc is present. The Nyquist plot deviates from an ideal circular shape due to non-ideal debye-type relaxation behavior. In the control 3D device, the low-frequency resistance increases significantly (Fig. 3d), suggesting electronic and ionic accumulation at the interfaces. This behavior indicates that the material is composed of conducting grains separated by poorly conducting grain boundaries. At low frequencies, electrons can traverse grain boundaries *via* hopping mechanisms, but high grain boundary resistance causes electron accumulation at the boundary, resulting in polarization. At high frequencies, electrons are unable to follow the rapid alternation of the applied field, reducing their accumulation at the grain boundaries. Consequently, the likelihood of electrons reaching the grain boundary decreases with increasing frequency, leading to reduced polarization. Additionally, the incorporation of BzCl and DFBzCl-based 2D layers on top of the 3D perovskite layer enhances polarization and increases interfacial resistance. We observed that the diameter of the small semicircle in the Nyquist plot increases in the BzCl and DFBzCl-modified 2D/3D devices (Fig. 3e), indicating a rise in resistance ($R(\omega) = \mathrm{Re}(Z)$), as also seen in the Bode plot. This increase in resistance is attributed to higher interfacial recombination and ionic migration resistance, which is more pronounced at lower frequencies.

The Nyquist plot shows that BzCl and DFBzCl modifications reduce ionic migration and interfacial recombination (Fig. 3e), which are crucial for achieving higher V_{OC}. The small semicircle at high frequencies indicates better charge separation and suppression of charge accumulation at interfaces. DFBzCl enhances the electric field at the interface, stabilizing the quasi-Fermi level splitting (QFLS) and reducing energy losses due to non-radiative recombination. In BzCl- and DFBzCl-modified films, the reduction in grain boundaries (as discussed previously) and improved film morphology facilitate more efficient charge transport across the perovskite layer. Reduced ionic migration and fewer defects (as shown by lower defect densities from Mott–Schottky analysis) ensure that fewer carriers are lost through non-radiative recombination or trapped at grain boundaries. As a result, more photogenerated carriers are collected at the electrodes, contributing to a higher J_{SC}. The improved interfacial properties and reduced ionic migration in the 2D/3D devices lead to lower series resistance (as seen in the impedance spectra). The reduction in ionic migration paths and better interface alignment minimize charge accumulation and hysteresis, allowing the device to operate closer to its MPP. Additionally, the suppression of interfacial recombination reduces parasitic losses, further contributing to a higher FF. The reduced hysteresis also ensures more stable operation and allows for more accurate power extraction, directly contributing to an improved FF. To further validate the data observed from Mott–Schottky and impedance analyses and correlate them with the device performance of 2D/3D PSCs, we measured the carrier decay lifetime using time-correlated single-photon counting (TCSPC), as shown in Fig. 3f. The obtained TCSPC curve was fitted using a three-exponential decay model, and the extracted lifetime parameters are presented in Table S2. It was observed that the DFBzCl-modified 2D/3D film exhibited a significantly prolonged carrier lifetime compared to both BzCl-modified and control films, indicating reduced recombination. This enhancement can be attributed to effective surface defect passivation, increased interfacial recombination resistance, and improved crystalline quality. The longer carrier lifetimes suggest that charge carriers have a higher probability of being extracted before undergoing recombination, leading to higher current density and overall device performance.

2.4 Excited state dynamics: transient absorption spectra of control and modified films

To further elucidate the improved performance of 2D/3D devices compared to the control 3D devices and to investigate the interaction between 2D and 3D perovskite films, along with their effect on the excited-state dynamics of the 3D perovskite and charge transfer processes to the transport layers, femtosecond transient absorption (TA) measurements were

conducted.[29,30,37] These measurements were performed on both neat control and modified perovskite films, as well as films with the PCBM ETL. The films were excited at 410 nm, and the TA signals were recorded in the probe range of 450 to 800 nm. The contour plot of the control film, control + 2D perovskite film with BzCl and with DFBzCl is shown in Fig. 4a–c, respectively. We have plotted the TA spectra at an earlier time up to 10 ps (Fig. 4d–f) and longer time up to 5 ns (Fig. 4g–i) to show the early time and longer time dynamics in these films. The TA spectra of the control film at early delay times (up to 10 ps) show a ground state bleach (GSB) band that is initially broadened up to 1.6 ps within the wavelength range of 550 nm to 750 nm, centred around 700 nm. This initial broadening is attributed to the thermal distribution of carriers across the available density of states.[46,47] After 1.6 ps, the GSB width starts to decrease, which is attributed to hot carrier cooling, where carriers in excited states relax from higher energy levels to the lowest energy level of the conduction band. In the case of BzCl modification, a reduction in the GSB width is observed, along with a redshift in the GSB position to approximately 740 nm (Fig. 4e). For the DFBzCl modification, an additional feature is observed: the appearance of a second small photobleach band around 625 nm and a third photobleach band around 550 nm, along with the 740 nm GSB band, persisting only up to 1.8 ps. The broader GSB observed in the control film can be attributed to the wide distribution of grain sizes. Additionally, the presence of localized states near the band edge, particularly at earlier times, contributes to the GSB broadening, likely causing carrier trapping.[43,48,49]

This implies that carriers populate a wider range of energy states in the density of states, leading to a broader bleaching effect. The reduction in GSB broadening in the modified films is ascribed to the passivation of shallow defects, which narrows the carrier distribution across the energy landscape. The observed redshift in the GSB peak position is likely a result of more delocalized electronic bands and the passivation of uncoordinated lead atoms at the surface. In contrast, the BzCl- and DFBzCl-modified films exhibit enhanced grain packing and a narrower grain size distribution, contributing to improved optoelectronic properties.[50] In the DFBzCl-modified film, additional GSB features around 625 nm observed at early times can be attributed to excitonic absorption, likely due to strong exciton binding arising from the 2D perovskite behavior.[47] Additionally, a peak around 550 nm is observed, which can be linked to the 2D layer-inducing bleaching effects. However, these effects diminish at longer time delays, indicating that exciton-related processes and the influence of the 2D layer are transient and primarily dominate the early-time dynamics.[41] At longer delay times, the TA spectra reveal that the GSB signal does not fully decay even up to 5 ns, indicating the presence of long-lived excited states as also observed from TCSPC data. The GSB width gradually decreases over time, and the GSB band undergoes a redshift, as shown in Fig. 4g. The redshift and

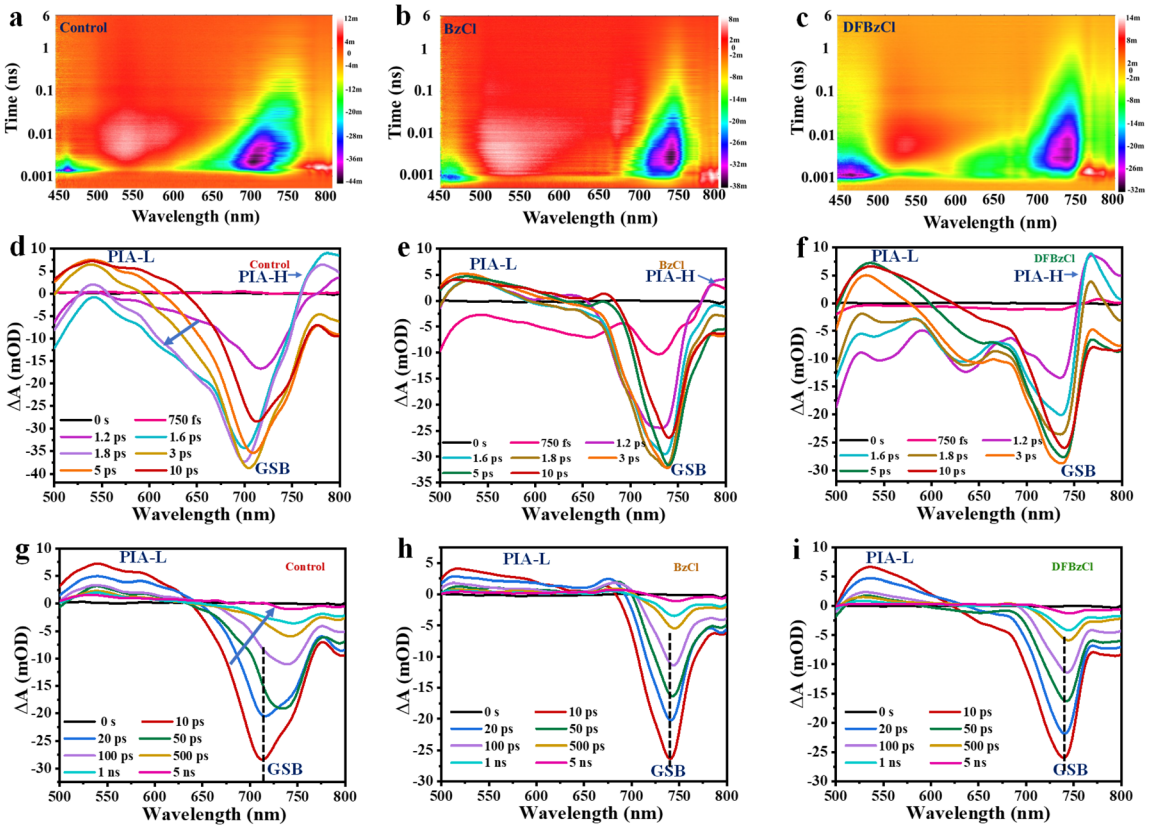

Fig. 4 Femtosecond transient absorption spectra of control 3D perovskite film and modified 2D/3D perovskite film. 2D contour plot of TA spectra (a) control, (b) modified with BzCl, and (c) modified with DFBzCl. Early time TA spectra up to 10 ps (d) control, (e) modified with BzCl and (f) modified with DFBzCl. Long delay time up to 5 ns TA spectra of (g) control, (h) modified with BzCl and (i) modified with DFBzCl.

narrowing indicate a relaxation of hot carriers towards lower energy states and reduced carrier population across various density ranges, likely due to carrier cooling and recombination. In the BzCl-modified film, the GSB is narrower compared to the control, and there is a broad photoinduced absorption (PIA-H) signal on the higher energy side, ranging from 500 nm to 670 nm (Fig. 4h). In the case of DFBzCl, the PIA broadness is reduced compared to BzCl (Fig. 4i). However, compared to the control film, the GSB width is reduced, and the position of the GSB is also redshifted. Interestingly, at earlier delay times, a PIA-L signal is observed on the lower energy side of the GSB in all three films. However, at longer delays, this PIA signal transitions into a GSB signal, indicating that the effects of bandgap renormalization and electron-phonon coupling are less pronounced in both the control and modified films.[51,52]

We found that charge extraction is efficient in 2D/3D devices as observed from the device efficiency data, which can be attributed to a three-step transport mechanism. First, photogenerated charge carriers in the 3D perovskite diffuse towards the 2D/3D interface. Next, lateral diffusion occurs, where the carriers move to regions where PCBM is in direct contact with the 3D perovskite. Since the 3D perovskite film is only partially covered by the 2D layer, sufficient exposed areas remain for effective charge extraction. This strategy is analogous to the design used in silicon solar cells, such as the passivated emitter rear contact (PERC) structure, where an insulating SiO_2 layer partially covers the silicon wafer, leaving certain regions open for charge transfer. To investigate the charge transport dynamics from the perovskite to the PCBM layer, we performed TA measurements on perovskite films with a PCBM layer.[53–55]

The contour plots for the control + PCBM, BzCl-modified + PCBM, and DFBzCl-modified + PCBM perovskite films are presented in Fig. 5a–c, respectively. Additionally, the early-time TA spectra (up to 10 ps) and the longer delay spectra (up to 5 ns) are shown in Fig. 5d–i for all films. The first notable observation is that the GSB band position in the control + PCBM film is centred at 750 nm, which is redshifted compared to the pristine control film. This redshift is consistent with that observed in the control and modified films without PCBM, suggesting that the 2D perovskite layer and PCBM suppress uncoordinated lead atoms and passivate surface defects.[53,56,57] Furthermore, the GSB band in the control + PCBM film shows reduced broadening compared to the pristine control film, indicating improved charge transport and passivation effects with the inclusion of the PCBM layer. The broadening of the high-energy tail, indicative of the non-equilibrium carrier distribution, is reduced in the perovskite + PCBM sample, suggesting that the treatment facilitates the extraction of hot carriers into PCBM.[56,58]

The kinetics of the ground-state bleaching (GSB) band for all films, both with and without PCBM, were analyzed by fitting

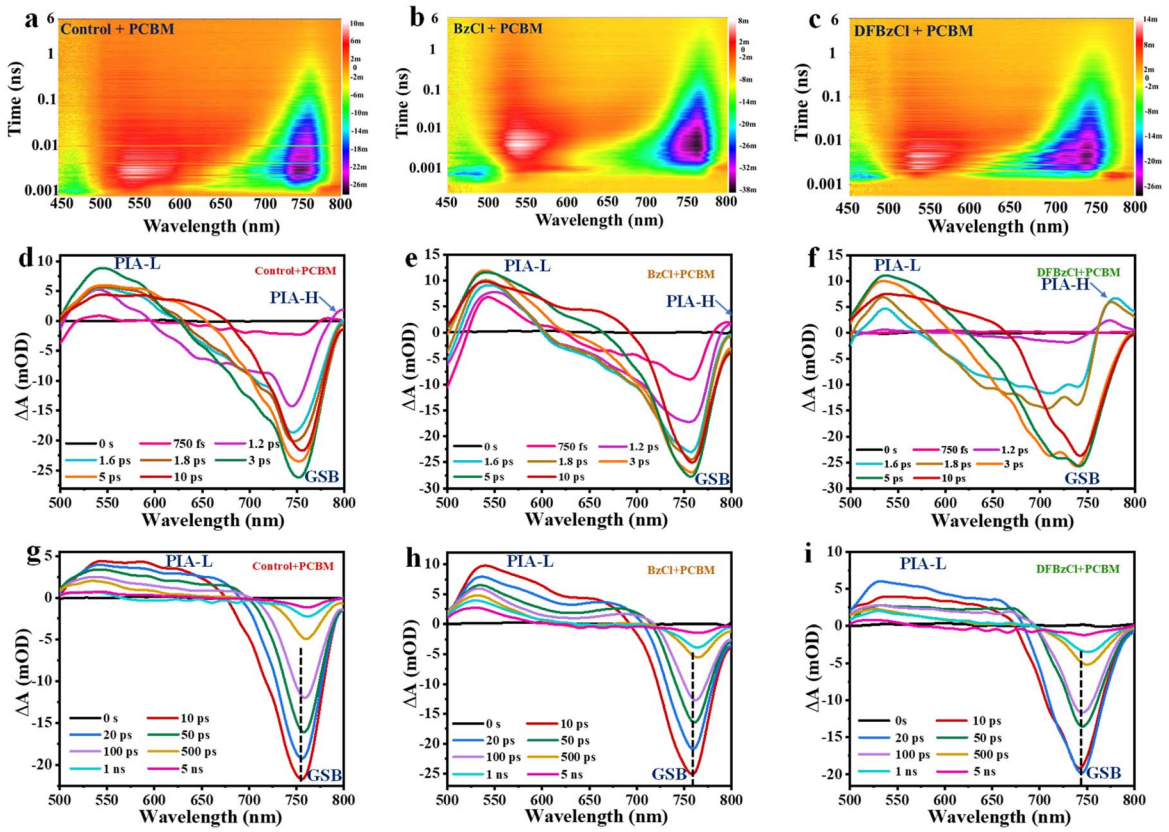

Fig. 5 Femtosecond transient absorption spectra of control 3D perovskite film and modified 2D/3D perovskite films with PCBM layer. 2D contour plot of TA spectra (a) control + PCBM, (b) BzCl + PCBM and (c) DFBzCl + PCBM. Early time TA spectra up to 10 ps (d) control + PCBM, (e) BzCl + PCBM and (f) DFBzCl + PCBM. Long delay time up to 5 ns TA spectra of (g) control + PCBM, (h) BzCl + PCBM and (i) DFBzCl + PCBM.

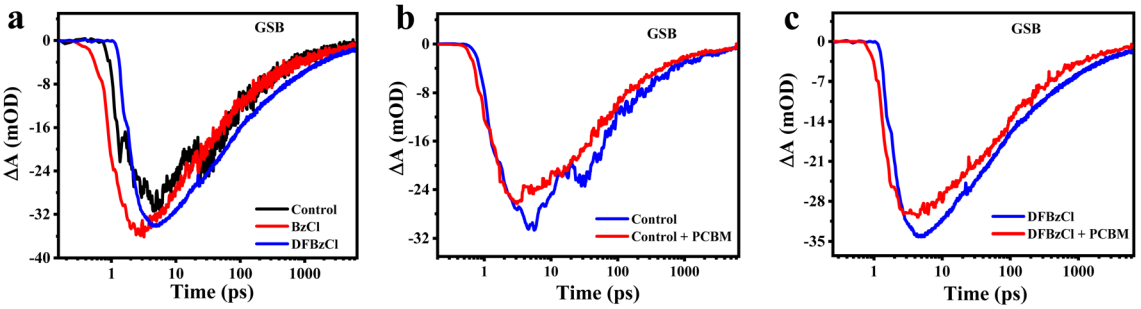

Fig. 6 TA Kinetics of GSB band of control and modified films with and without PCBM layer. (a) Comparison of GSB band kinetics of control, modified with BzCl and DFBzCl film. (b) GSB band kinetics of control and control + PCBM film. (c) GSB band kinetics of modified with DFBzCl and DFBzCl + PCBM film.

their decay dynamics (Fig. 6). The results indicate that the GSB recovery of the control film occurs at a faster rate compared to the BzCl- and DFBzCl-modified films. This suggests that the carrier relaxation process in the modified 2D/3D perovskite films is slower, implying more efficient carrier trapping or interaction with the lattice. Three distinct lifetime components were extracted from the GSB kinetics fitting (Fig. S20), as summarized in Table 2. The first component was found to be τ_1 = 14.3 ps for the control film, whereas it increased to τ_1 = 16.3 ps for the BzCl-modified film and τ_1 = 34.3 ps for the DFBzCl-modified film. This component is attributed to the hot carrier cooling time, which is prolonged in the 2D/3D perovskite films due to improved grain packing, lower trap density, and enhanced crystallization. These factors lead to increased band dispersion and a reduction in defects. Slower hot carrier cooling allows for the possibility of extracting carriers during this intermediate stage, thereby improving charge collection efficiency before non-radiative recombination occurs. The second component was found to be τ_2 = 108 ps and it is increased up to τ_2 = 340 ps for the DFBzCl-modified film, which can be attributed to charge trapping at shallow defects near the conduction band or uncoordinated lead atoms in the perovskite film, as inferred from the GSB width and position. In the control film, the fast decay implies that non-radiative recombination occurs more readily, reducing the number of carriers available for extraction. In contrast, the incorporation of BzCl and DFBzCl 2D capping layers reduces non-radiative recombination, likely due to structural modifications at the interface, enhanced uniformity in the film's morphology, and the presence of a built-in electric field. These factors improve the extraction of carriers during the initial stages of photoexcitation, ultimately contributing to enhanced carrier collection efficiency in the modified films.

Furthermore, the third-lifetime component (τ_3), which is linked to the band-to-band carrier decay, significantly increased from τ_3 = 1940 ps in the control film to τ_3 = 4000 ps in the DFBzCl-modified film.[59,60] Based on the lifetime data and reduced defect density, the 2D capping layer formed by BzCl and DFBzCl may increase carrier diffusion length compared to the control. This improvement is most likely due to the suppression of inherent non-radiative recombination processes, which are achieved by minimizing inelastic electron-phonon scattering. As a result, the 2D capping layers effectively promote longer carrier lifetimes and better charge transport within the films, which may contribute to improved device performance by reducing recombination losses and enhancing charge extraction efficiency. Furthermore, from the kinetics with PCBM, we observe a decrease in overall lifetime as GSB recovers faster in both the control + PCBM and DFBzCl-modified + PCBM films, indicating more efficient electron transfer to the PCBM layer. Transient absorption analysis reveals that incorporating a 2D layer on the 3D perovskite enhances hot carrier extraction, extends carrier decay lifetime, and improves charge transfer to the transport layer, all of which contribute to enhanced device performance.

Table 2 Extracted lifetime parameters from GSB band fitting of control, BzCl and DFBzCl modified film

Film	A_1 (%)	τ_1 (ps)	A_2 (%)	τ_2 (ps)	A_3 (%)	τ_3 (ps)
Control	70.8	14.3	22.5	108	7.75	1940
BzCl	47.1	16.3	37.3	139	15.6	2730
DFBzCl	50.3	34.3	34.3	340	15.4	4000

3 Conclusion

Here, we present a comprehensive investigation into the molecular interactions and excited-state dynamics that govern the performance and stability of 2D/3D PSCs utilizing MA-free "FA-Cs" perovskite structure. We found that incorporating the dipole moment on the perovskite layer in the form of 2D/3D perovskite can lead to significant enhancement in V_{OC} and device performance with DFBzCl-modified PSCs reaching PCE of 21.21%, compared to 18.09% for the control devices. Further supporting these findings, the Mott–Schottky analysis demonstrated a heightened built-in potential and reduced defect density in DFBzCl-based PSCs. Impedance spectroscopy also confirmed enhanced interfacial recombination resistance and reduced ion accumulation at the interface, while TCSPC measurements showed extended carrier lifetimes in DFBzCl-

treated devices, leading to minimized recombination losses and improved charge transport. Our detailed characterization, including ultrafast transient absorption spectroscopy, revealed that DFBzCl incorporation slows hot carrier cooling, increases charge transfer, minimizes phase segregation, and significantly extends carrier recombination lifetimes. These improvements are primarily driven by DFBzCl's higher dipole moment, which enhances the internal electric field, improves energy band alignment, and facilitates more efficient charge transport across the perovskite interface. The insights gained offer a strategic pathway for the rational design of next-generation PSCs, contributing to a deeper understanding of the fundamental photophysical processes that underpin high-performance solar cell operation.

Conflicts of interest

The authors declare no competing financial interest.

Data availability

The datasets generated and analysed during the current study are included in the published article and its supplementary information (SI) and source data files. Source data are provided with this paper. Supplementary information: experimental section; characterizations: XRD, UV-vis, PL, XPS, UPS, histogram plots of the average grain size, distribution curve obtained from KPFM, average surface potential distribution, cross-section SEM for control and modified films data and graphs, p-i-n solar cell statistics and operational stability, TA kinetics. See DOI: **https://doi.org/10.1039/d5el00121h**.

Acknowledgements

Shivani Choudhary acknowledges UGC fellowship. NKT acknowledges the grant GAL-2370-PHY. SS acknowledges SERB IRPHA project (SER-1852-PHY).

References

1 S. Li, Y. Jiang, J. Xu, D. Wang, Z. Ding, T. Zhu, B. Chen, Y. Yang, M. Wei, R. Guo, Y. Hou, Y. Chen, C. Sun, K. Wei, S. M. H. Qaid, H. Lu, H. Tan, D. Di, J. Chen, M. Gratzel, E. H. Sargent and M. Yuan, *Nature*, 2024, **635**, 82–88.
2 Y. Yang, C. Liu, Y. Ding, B. Ding, J. Xu, A. Liu, J. Q. Yu, L. Grater, H. H. Zhu, S. S. Hadke, V. K. Sangwan, A. S. R. Bati, X. B. Hu, J. T. Li, S. M. Park, M. C. Hersam, B. Chen, M. K. Nazeeruddin, M. G. Kanatzidis and E. H. Sargent, *Nat. Energy*, 2024, **9**, 316–323.
3 **https://www.nrel.gov/pv/cell-efficiency.html**.
4 M. I. Asghar, J. Zhang, H. Wang and P. D. Lund, *Renew. Sustain. Energy Rev.*, 2017, **77**, 131–146.
5 H. Yang, X. D. Li, X. M. Guo, C. Y. Lu, H. B. Yuan, A. Liu, W. X. Zhang and J. F. Fang, *ACS Energy Lett.*, 2023, **8**, 3793–3799.
6 Y. C. Liang, J. M. Xia, B. J. Fan, C. Liang, F. F. Yuan, S. H. Peng, Q. H. Sun, R. D. Zhao, Z. P. Miao, T. Zhang, H. Zhu, W. L. Liang, Y. H. Xie, S. F. Chen, X. T. Hu, Y. Q. Zhang, P. W. Li and Y. L. Song, *Nano Today*, 2024, **59**, 102479.
7 T. Liu, J. Guo, D. Lu, Z. Xu, Q. Fu, N. Zheng, Z. Xie, X. Wan, X. Zhang, Y. Liu and Y. Chen, *ACS Nano*, 2021, **15**, 7811–7820.
8 C. Tang, Y. Liu, Y. Zheng, A. Sun, J. Liang, X. Wu, C. Tian, Z. Li, J. Chen, J. Cai, X. Wu and C. C. Chen, *Small*, 2024, **20**, e2306978.
9 J. Wang, L. Bi, X. Huang, Q. Feng, M. Liu, M. Chen, Y. An, W. Jiang, F. R. Lin, Q. Fu and A. K. Y. Jen, *eScience*, 2024, **4**, 100308.
10 Z. Li, A. Sun, Y. Zheng, R. Zhuang, X. Wu, C. Tian, C. Tang, Y. Liu, B. Ouyang, J. Du, Z. Li, J. Cai, X. Wu, J. Chen, Y. Hua and C. C. Chen, *Small Methods*, 2024, e2400425.
11 X. Zang, S. Xiong, S. Jiang, D. Li, H. Wu, H. Ren, A. Cao, B. Li, Z. Ma, J. Chen, L. Ding, J. Tang, Z. Sun, J. Chu and Q. Bao, *Adv. Mater.*, 2024, **36**, e2309991.
12 G. Pica, R. Montecucco, A. Zanetta, A. Oranskaia, F. Faini, L. Pancini, N. Mrkyvkova, P. Siffalovic, P. Dally, V. Pirota, M. Ledinsky, M. De Bastiani, S. De Wolf, F. Doria, U. Schwingenschlögl and G. Grancini, *Sol. RRL*, 2024, **8**, 2300681.
13 Y. Zheng, C. Tian, X. Wu, A. Sun, R. Zhuang, C. Tang, Y. Liu, Z. Li, B. Ouyang, J. Du, Z. Li, X. Wu, J. Chen, J. Cai and C. C. Chen, *Adv. Energy Mater.*, 2024, **14**, 2304486.
14 Z. Z. Wang, T. F. Xu, N. Li, Y. L. Liu, K. Li, Z. H. Fan, J. K. Tan, D. H. Chen, S. Z. Liu and W. C. Xiang, *Energy Environ. Sci.*, 2024, **17**, 7271–7280.
15 X. Yue, X. Zhao, B. Fan, Y. Yang, L. Yan, S. Qu, H. Huang, Q. Zhang, H. Yan, P. Cui, J. Ji, J. Ma and M. Li, *Adv. Funct. Mater.*, 2022, **33**, 2209921.
16 Y. K. Qiu, J. H. Liang, Z. F. Zhang, Z. H. Deng, H. Xu, M. S. He, J. L. Wang, Y. J. Yang, L. T. Kong and C. C. Chen, *J. Phys. Chem. C*, 2021, **125**, 1256–1268.
17 X. Xu, Z. Zhang, T. Liu, P. Zhu, Z. Zhang and G. Xing, *J. Mater. Chem. A*, 2025, **13**(17), 12097–12103.
18 S. Min and J. Cho, *Adv. Opt. Mater.*, 2024, **12**, 2302516.
19 S. J. Yoon, M. Kuno and P. V. Kamat, *ACS Energy Lett.*, 2017, **2**, 1507–1514.
20 X. Li, W. Wang, P. Huang, L. Yang, J. Hu, K. Wei, L. Gao, Y. Jiang, K. Sun, G. Du, X. Cai, C. Liu, W. Tang and J. Zhang, *Adv. Sci.*, 2024, **11**, e2403735.
21 T. Zhou, Q. Li and L. Zhou, *Adv. Energy Mater.*, 2024, **14**, 2400050.
22 H. Zhang, W. Xiang, X. Zuo, X. Gu, S. Zhang, Y. Du, Z. Wang, Y. Liu, H. Wu, P. Wang, Q. Cui, H. Su, Q. Tian and S. F. Liu, *Angew. Chem.*, 2023, **62**, e202216634.
23 M. C. Gélvez-Rueda, S. Peeters, P. C. Wang, K. M. Felter and F. C. Grozema, *Helv. Chim. Acta*, 2020, **103**, e2000121.
24 E. Jung, K. Budzinauskas, S. Öz, F. Ünlü, H. Kuhn, J. Wagner, D. Grabowski, B. Klingebiel, M. Cherasse, J. W. Dong, P. Aversa, P. Vivo, T. Kirchartz, T. Miyasaka, P. H. M. van Loosdrecht, L. Perfetti and S. Mathur, *ACS Energy Lett.*, 2020, **5**, 785–792.
25 C. B. Li, A. L. Wang, X. Y. Deng, S. R. Wang, Y. Yuan, L. M. Ding and F. Hao, *ACS Photonics*, 2020, **7**, 1893–1907.

26 J. Wu, H. Cha, T. Du, Y. Dong, W. Xu, C. T. Lin and J. R. Durrant, *Adv. Mater.*, 2022, **34**, e2101833.
27 W. Shen, Z. Wu, G. Yang, Y. Kong, W. Li, G. Liang, F. Huang, Y. B. Cheng and J. Zhong, *J. Phys. Chem. Lett.*, 2022, **13**, 3188–3196.
28 C. M. Wolff, S. A. Bourelle, L. Q. Phuong, J. Kurpiers, S. Feldmann, P. Caprioglio, J. A. Marquez, J. Wolansky, T. Unold, M. Stolterfoht, S. Shoaee, F. Deschler and D. Neher, *Adv. Energy Mater.*, 2021, **11**, 2101823.
29 S. Srivastava, S. Ranjan, L. Yadav, T. Sharma, S. Choudhary, D. Agarwal, A. Singh, S. Satapathi, R. K. Gupta, A. Garg and K. S. Nalwa, *Commun. Mater.*, 2023, **4**, 52.
30 S. Choudhary, R. Garai, R. K. Gupta, M. A. Afroz, T. Sharma, Yukta, B. Sharma, P. K. Iyer and S. Satapathi, *ACS Appl. Energy Mater.*, 2024, **7**, 3709–3717.
31 S. Choudhary, N. C. Maurya, N. K. Tailor, K. V. Adarsh and S. Satapathi, *Small*, 2025, **21**, e2406365.
32 X. Liang, X. Zhou, F. Wang, H. Chen, D. Duan, K. Zhou, C. Ge, J. Xiang, J. Zhu, D. Wang, Q. Zhu, H. Lin, C. H. Lin, Y. Shi, G. Xing, H. Hu and T. Wu, *Adv. Energy Mater.*, 2024, **14**, 2402243.
33 R. K. Gupta, R. Garai, B. Sharma, M. A. Afroz, S. Choudhary, P. K. Iyer and S. Satapathi, *Energy Fuels*, 2022, **37**, 667–674.
34 Y. Zhang, M. Chen, T. He, H. Chen, Z. Zhang, H. Wang, H. Lu, Q. Ling, Z. Hu, Y. Liu, Y. Chen and G. Long, *Adv. Mater.*, 2023, **35**, e2210836.
35 J. Wang, Z. Zhang, J. Liang, Y. Zheng, X. Wu, C. Tian, Y. Huang, Z. Zhou, Y. Yang, A. Sun, Z. Chen and C. C. Chen, *Small*, 2022, **18**, e2203886.
36 R. F. Moral, C. A. R. Perini, T. Kodalle, A. Kim, F. Babbe, N. Harada, J. Hajhemati, P. Schulz, N. S. Ginsberg, S. Aloni, C. P. Schwartz, J. P. Correa-Baena and C. M. Sutter-Fella, *ACS Energy Lett.*, 2024, **9**, 2703–2716.
37 H. Gu, A. Zhu, J. Xia, W. Li, J. Zheng, T. Yang, S. Li, N. Zhang, S. Mei, Y. Cai, S. Chen, C. Liang and G. Xing, *Sci. Bull.*, 2024, **69**, 2853–2861.
38 T. Wang, L. Bi, L. Yang, Z. Zeng, X. Ji, Z. Hu, S. W. Tsang, H. L. Yip, Q. Fu, A. K. Jen and Y. Liu, *J. Am. Chem. Soc.*, 2024, **146**, 7555–7564.
39 Y. Zhang and N.-G. Park, *ACS Energy Lett.*, 2022, **7**, 757–765.
40 T. H. Yang, C. Ma, W. L. Cai, S. Q. Wang, Y. Wu, J. S. Feng, N. Wu, H. J. Li, W. L. Huang, Z. C. Ding, L. L. Gao, S. Z. Liu and K. Zhao, *Joule*, 2023, **7**, 574–586.
41 J. Hu, C. Wang, S. Qiu, Y. Zhao, E. Gu, L. Zeng, Y. Yang, C. Li, X. Liu, K. Forberich, C. J. Brabec, M. K. Nazeeruddin, Y. Mai and F. Guo, *Adv. Energy Mater.*, 2020, **10**, 2000173.
42 T. T. Li, J. Xu, R. X. Lin, S. Teale, H. J. Li, Z. Liu, C. Y. Duan, Q. Zhao, K. Xiao, P. Wu, B. Chen, S. Jiang, S. B. Xiong, H. W. Luo, S. S. Wan, L. D. Li, Q. Y. Bao, Y. X. Tian, X. P. Gao, J. Xie, E. H. Sargent and H. R. Tan, *Nat. Energy*, 2023, **8**, 610–620.
43 Y. Zheng, X. Wu, R. Zhuang, C. Tian, A. Sun, C. Tang, Y. Liu, Y. Hua and C. C. Chen, *Adv. Funct. Mater.*, 2023, **33**, 2300576.
44 Q. H. Li, H. Liu and T. Zhou, *Sci. China Chem.*, 2024, **67**, 3083–3090.
45 Y. M. Li, Z. J. Chen, B. C. Yu, S. Tan, Y. Q. Cui, H. J. Wu, Y. H. Luo, J. J. Shi, D. M. Li and Q. B. Meng, *Joule*, 2022, **6**, 676–689.
46 T. Niu, J. Lu, X. Jia, Z. Xu, M. C. Tang, D. Barrit, N. Yuan, J. Ding, X. Zhang, Y. Fan, T. Luo, Y. Zhang, D. M. Smilgies, Z. Liu, A. Amassian, S. Jin, K. Zhao and S. Liu, *Nano Lett.*, 2019, **19**, 7181–7190.
47 P. Li, Y. Zhang, C. Liang, G. Xing, X. Liu, F. Li, X. Liu, X. Hu, G. Shao and Y. Song, *Adv. Mater.*, 2018, **30**, e1805323.
48 T. Kodalle, R. F. Moral, L. Scalon, R. Szostak, M. Abdelsamie, P. E. Marchezi, A. F. Nogueira and C. M. Sutter-Fella, *Adv. Energy Mater.*, 2022, **13**, 2201490.
49 G. Y. Yang, Y. B. Tu, J. C. Ye, R. C. Liu, Y. Zang, L. J. Zhang, Y. Wang, G. D. Li, Q. Zhou, L. Chu and W. S. Yan, *J. Alloys Compnd.*, 2023, **952**, 170051.
50 M. Singh, I. H. Ho, A. Singh, C. W. Chan, J. W. Yang, T. F. Guo, H. Ahn, V. C. Tung, C. W. Chu and Y. J. Lu, *ACS Photonics*, 2022, **9**, 3584–3591.
51 D. P. Panda, D. Swain, M. Chaudhary, S. Mishra, G. Bhutani, A. K. De, U. V. Waghmare and A. Sundaresan, *Inorg. Chem.*, 2022, **61**, 17026–17036.
52 R. Kentsch, M. Scholz, J. Horn, D. Schlettwein, K. Oum and T. Lenzer, *J. Phys. Chem. C*, 2018, **122**, 25940–25947.
53 M. Zhou, J. S. Sarmiento, C. B. Fei and H. Wang, *J. Phys. Chem. C*, 2019, **123**, 22095–22103.
54 K. Pydzinska, J. Karolczak, I. Kosta, R. Tena-Zaera, A. Todinova, J. Idigoras, J. A. Anta and M. Ziolek, *ChemSusChem*, 2016, **9**, 1647–1659.
55 J. Horn, I. Minda, H. Schwoerer and D. Schlettwein, *Phys. Status Solidi B*, 2018, **256**, 1800265.
56 J. I. Khan, F. H. Isikgor, E. Ugur, W. Raja, G. T. Harrison, E. Yengel, T. D. Anthopoulos, S. De Wolf and F. Laquai, *ACS Energy Lett.*, 2021, **6**, 4155–4164.
57 I. Levine, A. Al-Ashouri, A. Musiienko, H. Hempel, A. Magomedov, A. Drevilkauskaite, V. Getautis, D. Menzel, K. Hinrichs, T. Unold, S. Albrecht and T. Dittrich, *Joule*, 2021, **5**, 2915–2933.
58 E. Ugur, J. I. Khan, E. Aydin, M. Wang, M. Kirkus, M. Neophytou, I. McCulloch, S. De Wolf and F. Laquai, *J. Phys. Chem. Lett.*, 2019, **10**, 6921–6928.
59 F. Wang, X. Y. Jiang, H. Chen, Y. Q. Shang, H. F. Liu, J. L. Wei, W. J. Zhou, H. L. He, W. M. Liu and Z. J. Ning, *Joule*, 2018, **2**, 2732–2743.
60 J. S. Manser and P. V. Kamat, *Nat. Photonics*, 2014, **8**, 737–743.